



Ground Moving Target Indication for the Geosynchronous-Low Earth Orbit Bistatic Multichannel SAR System

Shuangxi Zhang , Member, IEEE, Yuxin Gao, Mengdao Xing , Fellow, IEEE, Rui Guo, Member, IEEE, Junli Chen, and Yanyang Liu

I. INTRODUCTION

Abstract—In this article, an effective clutter suppression and moving target imaging approach is proposed for the geosynchronous-low earth orbit (GEO-LEO) bistatic multichannel synthetic aperture radar (SAR) system, which is robust for the fast moving target with Doppler centroid ambiguity. For the GEO-LEO bistatic multichannel SAR system, the characteristic of baseline with azimuth invariant in Doppler Fourier transform domain is not tenable. It is difficult to implement clutter suppression by the unified baseline compensation in azimuth Doppler Fourier transform domain. Fortunately, we discover that the baseline can be approximately regarded as a constant in chirp Fourier transform domain for the GEO-LEO bistatic multichannel SAR system. Hence, the corresponding baseline compensation can be achieved in the azimuth chirp Fourier transform domain for the clutter. With an orthogonality vector of clutter, the clutter can be well suppressed and the moving target is extracted. After that, the moving target imaging approach is developed with the baseband Doppler centroid estimation and Doppler ambiguity number estimation. Finally, the theoretical investigations and the proposed approach in this article are validated by some experiments, where the experiments for clutter suppression and experiments for fast moving targets are included. Especially, an experiment with real SAR scattering scene is involved. In addition, some discussions for blind velocity targets are presented.

Index Terms—Bistatic multichannel synthetic aperture radar (SAR), blind velocity, chirp Fourier transform, clutter suppression, Doppler centroid ambiguity, Doppler centroid estimation, geosynchronous-low earth orbit (GEO-LEO).

Manuscript received March 12, 2021; revised April 16, 2021; accepted April 27, 2021. Date of publication May 3, 2021; date of current version May 26, 2021. This work was supported in part by Shaanxi Provincial Innovation Capability Support Program under Grant 2020KJXX-029, in part by the National Natural Science Foundation of China under Grant 61801387 and Grant 61771395, in part by China Postdoctoral Science Foundation under Grant 2019M653741, in part by the Aeronautical Science Foundation of China under Grant ASFC-20182053022, in part by the Shanghai Aerospace Science and Technology Innovation Foundation under Grant SAST2020-029, and in part by the Equipment Preresearch Foundation under Grant 61404130125. (Corresponding author: Shuangxi Zhang.)

Shuangxi Zhang is with the School of Electronics and information, Northwestern Polytechnical University, Xi'an 710071, China, and also with Toll Microelectronic, Xi'an 710075, China (e-mail: shuangxizhang1984@163.com).

Yuxin Gao and Rui Guo are with the School of Electronics and Information, Northwestern Polytechnical University, Xi'an 710071, China (e-mail: gaoyuxin@mail.nwpu.edu.cn; gr2003@nwpu.edu.cn).

Mengdao Xing is with the National Key Lab of Radar Signal Processing, Xidian University, Xi'an 710071, China (e-mail: xing_xmd@xidian.edu.cn).

Junli Chen and Yanyang Liu are with the Shanghai Institute of Satellite Engineering, Shanghai 200090, China (e-mail: 13917308065@139.com; yanyangliu0510@163.com).

Digital Object Identifier 10.1109/JSTARS.2021.3077003

SINCE the bistatic synthetic aperture radar (SAR) has the capability of acquiring more scenario information than monostatic radar, great interests have grown considerably in the last decades [1], [2]. In particular, the peculiarities of a bistatic configuration for the multichannel ground moving target indication (GMTI) have drawn the attention of radar system design and signal processing researchers. Considering that the geosynchronous earth orbit SAR (GEO-SAR) is capable of imaging a continuous planetary area wide ground swath, the bistatic SAR consisting of a GEO transmitter and a low-earth-orbit (LEO) multichannel receiver is proposed to obtain the high-resolution and wide-swath earth observation image [3]–[5]. With the GMTI technique [1], [2], [6],[7] and the advantages of GEO-LEO radar system, the GEO-LEO bistatic multichannel SAR-GMTI system will be presented in this article. Then, the corresponding key techniques will be discussed, including the clutter suppression and moving target imaging processing, etc.

Some available clutter suppression approaches have been proposed for the SAR-GMTI system. One of the most effective clutter suppression methods is the space-time adaptive processing (STAP), where a 2-D adaptive filter is constructed in both the temporal and spatial domain to suppress ground clutter [8]–[14]. However, for a nonhomogeneous environment, the covariance matrix cannot be effectively estimated and the performance of the corresponding STAP processor is degraded. At the same time, the great computation burden is brought by the STAP processing and more than two channel freedom is required. For the clutter suppression of two-channel radar systems, the displaced-phase-center antenna (DPCA) [15] and along-track interferometry (ATI) [16] were designed. When the two antennas move in the azimuth direction, the signal of two different antennas has an operation of subtracting for the DPCA approach and the phase difference information of the two antennas is employed to detect targets for ATI algorithm [17], [18]. In addition, a linear phase compensation in the azimuth Fourier transform domain is required for the single-static radar system, when the interval between the two antennas (is called as baseline length) is not equal to the platform movement distance during integral times of pulse time. Since the baseline length varies with the scene for the bistatic SAR system, the existing DPCA approach cannot be directly employed for the bistatic multichannel SAR system.

In this article, based on the orthogonality vector technique, an effective clutter suppression is developed for the GEO-LEO bistatic multichannel SAR-GMTI (GEO-LEO MC-SAR-GMTI) system, where the chirp Fourier transform is involved. For the conventional single-static multichannel SAR system, the distance between the transmitted antenna and received antenna is short enough to employ the equivalent phase center (EPC) approach. After the EPC processing, the signal can be regarded as being transmitted and received at the middle position between the transmitted antenna and received antenna. Then, the along track baseline has a characteristic of azimuth invariant in azimuth Doppler Fourier transform domain and the baseline compensation is effectually implemented. However, for the GEO-LEO MC-SAR-GMTI system, the baseline between the transmitted antenna and received is very long. When the EPC technique is adopted, an error is induced and varies with clutter scene, which is difficult to compensate. If the error is not well calibrated, the clutter cannot be well suppressed. Fortunately, when the quadratic phase of azimuth slow time is dispelled for the GEO-LEO bi-static SAR-GMTI echo, the linear and constant phase will remain. Note that there is approximately an equivalent time delay brought by the baseline length, where the time delay can be regarded as a constant. According to the signal processing theory, a constant time delay can be compensated in Fourier domain with a linear phase. The quadratic phase compensation with azimuth Fourier transform is called as the azimuth chirp Fourier transform. Based on the discussion above, the clutter suppression processing is implemented in azimuth chirp Fourier transform for the GEO-LEO bistatic SAR-GMTI system. First, a quadratic phase compensation is implemented, where the time delay brought by the baseline length for the slant-range of LEO-SAR is involved. Then, an equivalent linear phase compensation is implemented after azimuth Fourier transform. After the phase compensation, the vector corresponding to clutter is available. The orthogonality vector can be constructed by the clutter vector. With the orthogonality vector of clutter, the clutter can be well suppressed and the moving target echo can be extracted. The azimuth Fourier transform and the suppressing clutter with orthogonality vector are both the crucial steps for the proposed clutter suppression approach.

Combining the clutter suppression approach, the corresponding moving target imaging approach is presented in this article, where the Doppler centroid correction, azimuth inverse-chirp Fourier transform and keystone transform are involved. After the clutter suppression, the extracted moving target echo presents high signal-to-noise ratio (SNR), linear range cell migration (LRCM), and quadratic range cell migration (QRCM). During moving target imaging processing, the LRCM and QRCM must be corrected. Since the geometry of GEO-LEO MC-SAR-GMTI system is complex and the moving target is noncooperative, the imaging approach based on parameters estimation is proposed. First, the Doppler centroid is estimated and employed to implement the LRCM correction. After that, the minimum entropy approach is adopted to estimate the Doppler chirp rate. Then, the QRCM can be well corrected in the azimuth slow time, where the quadratic phase is eliminated. When the moving target does not locate on the center in the scene, an equivalent LRCM is brought. Hence, the keystone is adopted to correct the induced LRCM.

After the azimuth Doppler Fourier transform, the focused moving target image can be obtained. Since the Doppler centroid ambiguity number can be estimated during imaging processing, the presented moving target imaging approach is robust for the fast moving target.

The remainder of this article is organized as follows. In Section II, the signal model of a GEO-LEO bistatic multichannel SAR system is presented, where the signal of clutter and moving target are both discussed. Then, the clutter suppression approach is shown in detail in Section III. In addition, the imaging processing for moving target is given in Section IV. In Section V, the effectiveness of the proposed clutter suppression and moving target imaging approach is demonstrated via simulated data. In addition, the discussion for blind velocity is also shown. Finally, the conclusion is drawn in Section VI.

II. SIGNAL MODEL

In this section, the GEO-LEO bi-static SAR-GMTI system will be presented, and some advantages will be introduced. Then, the signal model of a GEO-LEO MC-SAR-GMTI system will be discussed for the clutter and the moving targets, where the multichannel GEO-LEO geometry and slant-range approximate are included.

A. GEO-LEO MC-SAR-GMTI System

For the GEO-LEO MC-SAR-GMTI system, the capability of wide-area continuous illumination is offered by the GEO-SAR system and the LEO multichannel receivers is employed to provide the performance for the clutter suppression and moving target detection. In addition, compared with the GEO monostatic SAR system, the LEO can obtain the higher SNR and finer spatial resolution with less power consumption and lower system complexity. At the same time, some advantages, such as good flexibility, antiattack, and well concealment etc., are provided by the GEO-LEO MC-SAR-GMTI system. In summary, the main contributions of the GEO-LEO MC-SAR-GMTI system are fourfold.

- 1) The system has the capability of suppressing clutter, detecting moving target and implementing indication for ground moving target.
- 2) The system shows a good flexibility and obtains the observation of moving targets with different angles. For some moving targets, the system can obtain a higher radar cross section (RCS) than a monostatic radar system. At the same time, it has the capability of anti-attack and good concealment.
- 3) The system strikes a balance between SNR and wide swath. For the GEO-SAR, it has the capability of wide swath observation. The LEO-SAR system can obtain the high SNR image with less power consumption. Hence, the GEO-LEO bistatic multichannel SAR system can obtain a middle SNR image with middle power consumption when the requirement of wide swath is satisfied.
- 4) For the multichannel in azimuth SAR-GMTI system, the system platform has a higher corresponding blind velocity

and a minimum detection velocity. The velocity of GEO-SAR platform is low, while the velocity of LEO-SAR platform is high. Hence, the GEO-LEO bistatic multichannel SAR system can obtain a middle blind velocity and middle minimum detection velocity.

B. Signal Model for Clutter

Similar to the GEO-LEO bistatic multichannel HRWS SAR system [3], [19], an accurate geometry of a GEO-LEO bistatic multichannel SAR system is presented in Fig. 9. Then, the details are discussed in Appendix A, where the approximate geometry of GEO-SAR or LEO-SAR is given. After that, the approximate geometry of a GEO-LEO bistatic multichannel SAR system is presented in Fig. 1, where the GEO platform is employed to transmit the chirp signal with a velocity of V_T , squint angle θ_T , the beam center slant-range R_T for the point target P in the imaging scene center, and the LEO platform is employed to receive the echo with a velocity of V_r , squint angle θ_r , the beam center slant-range R_r for the corresponding point target P .

Let t_m be the azimuth slow time, the slant-range between the transmitted antenna of the GEO platform with a position of $(X_0 + at_m, Y_0 + bt_m, Z_0 + et_m)$ and the clutter target with a position of $(x_i, y_i, 0)$ can be expressed as

$$R_T(t_m) = \sqrt{R_T^2 - 2R_T V_T \left(t_m - \frac{x_i}{V_T}\right) \sin \theta_T + V_T^2 \left(t_m - \frac{x_i}{V_T}\right)^2} \quad (1)$$

where $(X_0 + at_m, Y_0 + bt_m, Z_0 + et_m)$ denotes the position vector for $t_m=0$, (a, b, e) is the velocity vector for the GEO platform. For the low squint mode, (1) can be re-expressed as

$$R_T(t_m) \approx R_T - V_T \sin \theta_T \left(t_m - \frac{x_i}{V_T}\right) + k_T \left(t_m - \frac{x_i}{V_T}\right)^2 \quad (2)$$

where $k_T = \frac{V_T^2 \cos^2 \theta_T}{2R_T}$. When the hypothesis of ‘‘go and stop’’ does not hold, the slant-range between the n th received antenna of the LEO platform with a position of $(Vt_m + d_n, 0, H)$ and the target in the imaging scene is described as

$$R_{r,n}(t_m) = \left\{ R_r^2 - 2R_r V_r \left(t_m + \Delta T - \frac{x_i}{V_r} - \frac{d_n}{V_r}\right) \sin \theta_T + V_r^2 \left(t_m + \Delta T - \frac{x_i}{V_r} - \frac{d_n}{V_r}\right)^2 \right\}^{\frac{1}{2}} \quad (3)$$

where

$$\Delta T = \frac{R_T(t_m) + R_r(t_m)}{c} \approx \frac{R_T + R_r}{c}. \quad (4)$$

A discussion about the approximation in (4) is presented in Appendix B. c is the velocity of electromagnetic propagation. With the Taylor approximation, $R_{r,n}(t_m)$ is expanded as

$$R_{r,n}(t_m) \approx R_r - V_r \sin \theta_T \left(t_m - \frac{x_i}{V_r} - \frac{d_n}{V_r}\right) + k_r \left(t_m - \frac{x_i}{V_r} - \frac{d_n}{V_r}\right)^2 - \varphi_r \left(t_m - \frac{x_i}{V_r} - \frac{d_n}{V_r}\right) + \Delta R_r \quad (5)$$

where

$$\Delta R_r = V_r \cdot \frac{(R_r + R_T)}{c} \cdot \sin \theta_T + k_r \cdot \left(\frac{(R_r + R_T)}{c}\right)^2 \quad (6.a)$$

$$\varphi_r = \frac{V_r^2 \cos^2 \theta_T}{R_r} \cdot \frac{(R_r + R_T)}{c} \quad (6.b)$$

$$k_r = \frac{V_r^2 \cos^2 \theta_T}{2R_r}. \quad (6.c)$$

Let \hat{t} denote the range fast time, γ be the chirp signal rate of transmitted signal, f_c be carrier frequency, and λ denote the wavelength. After the range Fourier transform, the n th channel echo of clutter is expressed as

$$SS_n^c(f_r, t_m) = W_r(f_r) w_a(t_m) \exp\left(-j\pi \frac{f_r^2}{\gamma}\right) \cdot \exp\left[-j2\pi \frac{(f_c + f_r) \cdot (R_T(t_m) + R_{r,n}(t_m))}{c}\right] \quad (7)$$

where $W_r(f_r)$ is the respective range pulse envelope in the range frequency domain and $w_a(t_m)$ is the antenna beam modulation in azimuth slow time domain.

C. Signal Model for Moving Target

Assume that the moving target has an along GEO platform trajectory velocity of $v_{T,a}$ and an along transmitted beam center line direction velocity of $v_{T,r}$. The slant-range between the transmitted antenna of the GEO platform and the moving target in the imaging scene is

With Taylor series expanded, (8) shown at the bottom of this page can be rewritten as

$$R_T(t_m) \approx R_T + v_{T,r} \left(t_m - \frac{x_i}{V_T}\right) - (V_T + v_{T,a}) \left(t_m - \frac{x_i}{V_T}\right) \sin \theta_T + k_{T_mov} \cdot \left(t_m - \frac{x_i}{V_T}\right)^2 \quad (9)$$

$$R_T(t_m) = \left\{ \left(R_T + v_{T,r} \left(t_m - \frac{x_i}{V_T}\right)\right)^2 + (V_T + v_{T,a})^2 \left(t_m - \frac{x_i}{V_T}\right)^2 - 2 \left(R_T + v_{T,r} \left(t_m - \frac{x_i}{V_T}\right)\right) (V_T + v_{T,a}) \left(t_m - \frac{x_i}{V_T}\right) \sin \theta_T \right\}^{\frac{1}{2}}. \quad (8)$$

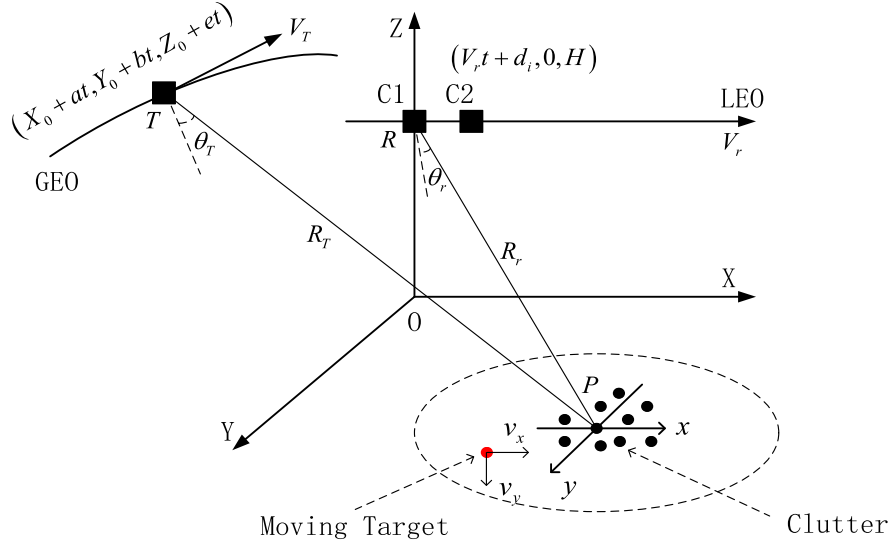


Fig. 1. Approximate geometry for the GEO-LEO MC-SAR-GMTI system.

where $k_{T_mov} = \frac{(V_T + v_{T,a})^2}{2R_T} \cos^2 \theta_T$. The slant-range between the n th received antenna of the LEO platform and the moving target in the imaging scene can be expressed as where $v_{r,r}$ denotes the moving target with an along received beam center line direction velocity, $v_{a,r}$ is the moving target with an along LEO platform trajectory velocity. Then, (10) shown at the bottom of this page can be re-expressed as where (11).

$$\Delta R_r^{mov} = -\frac{(R_T + R_r)}{c} (v_{r,r} - (V_r + v_{a,r}) \cdot \sin \theta_r) + \frac{(V_r + v_{a,r})^2}{2R_r} \left(\frac{(R_T + R_r)}{c} \right)^2 \quad (12.a)$$

$$\varphi_r^{mov} = \frac{(V_r + v_{a,r})^2}{R_r} \frac{(R_r + R_T)}{c} \quad (12.b)$$

$$k_{r_mov} = \frac{(V_r + v_{a,r})^2}{2R_r} \cos^2 \theta_r \quad (12.c)$$

Hence, the n th channel echo for the moving target can be described as where

$$M_a(f_r) = \exp \left[-j2\pi \frac{(f_c + f_r) \cdot (R_T + R_r + \Delta R_T)}{c} \right]. \quad (14)$$

III. CLUTTER SUPPRESSION

In this section, we will focus on discussing the clutter suppression approach. First, the chirp Fourier transform technique is employed to obtain the coarse-focused SAR image for the clutter. Then, the clutter suppression approach is presented. Finally, the signal model of the moving target will be discussed after the clutter suppression.

A. Chirp Fourier Transform for Clutter Echo and Clutter Suppression

From (13) as shown at the bottom of the next page, RCMC and range compression function of the n th channel in the range frequency and azimuth time domain can be expressed as

$$H_{n,1}(f_r, t_m) = \exp \left(j\pi \frac{f_r^2}{\gamma} \right) \cdot \exp \left[j2\pi \frac{(f_c + f_r)}{c} \cdot \left((-\varphi_c - V_r \sin \theta_r) \left(t_m - \frac{d_n}{V_r} \right) - V_T \sin \theta_T t_m \right) \right]. \quad (15)$$

After the RCMC and range compression with (15), the n th channel echo of clutter can be described as (16).

$$R_{r,n}(t_m) = \left\{ \left(R_r + v_{r,r} \left(t_m - \Delta T - \frac{x_i}{V_r} \right) \right)^2 + (V_r + v_{a,r})^2 \left(t_m - \Delta T - \frac{x_i}{V_r} - \frac{d_n}{V_r} \right)^2 - 2 \left(R_r + v_{r,r} \left(t_m - \Delta T - \frac{x_i}{V_r} \right) \right) (V_r + v_{a,r}) \left(t_m - \Delta T - \frac{x_i}{V_r} - \frac{d_n}{V_r} \right) \sin \theta_r \right\}^{\frac{1}{2}} \quad (10)$$

$$R_{r,n}(t_m) = R_r + v_{r,r} \left(t_m - \frac{x_i}{V_r} \right) - (V_r + v_{a,r}) \left(t_m - \frac{x_i}{V_r} - \frac{d_n}{V_r} \right) \sin \theta_r + k_{r_mov} \cdot \left(t_m - \frac{x_i}{V_r} - \frac{d_n}{V_r} \right)^2 - \varphi_r^{mov} \left(t_m - \frac{x_i}{V_r} - \frac{d_n}{V_r} \right) + \Delta R_r^{mov} \quad (11)$$

From (16) as shown at the bottom of this page, $k_r(t_m - \frac{d_n}{V_r} - \frac{x_i}{V_r})^2$ contains the baseline. $k_T(t_m - \frac{x_i}{V_T})^2$ is independent of the baseline. It is difficult to obtain a uniform time delay brought by baseline for (16). In other words, the baseline in clutter echo varies with scene. In order to eliminate the variance of baseline, the quadratic phase is removed. A kernel function for removing quadratic phase in (16) is constructed as

$$H_{n,2}(f_r, t_m) = \exp \left[j2\pi \frac{(f_c + f_r)}{c} \cdot \left(k_T t_m^2 + k_r \left(t_m - \frac{d_n}{V_r} \right)^2 \right) \right]. \quad (17)$$

The kernel function shown in (17) is multiplied to the clutter echo. After the azimuth Fourier transform, the n th channel clutter echo is rewritten (18) as shown at the bottom of this page, where $\eta_c = \frac{V_r \cos^2 \theta_r}{\frac{V_T \cos^2 \theta_T + V_r \cos^2 \theta_r}{R_T}}$, $W_a(f_a)$ denotes the window function in azimuth Doppler domain, corresponding to the envelope of the Fourier transform for $w_a(t_m)$. The operation above is called as the azimuth chirp Fourier transform. Note that the equivalent baseline of $\eta_c \cdot d_n$ is a constant. The corresponding time delay is $\eta_c \cdot (\frac{d_n}{V_r})$. Hence, the equivalent time delay can be well compensated. In the range frequency and azimuth chirp Fourier transform domain, a phase compensation function for the n th channel can be constructed as

$$H_{n,3}(f_r, f_a) = \exp \left(j2\pi f_a \eta_c \cdot \left(\frac{d_n}{V_r} \right) \right). \quad (19)$$

After the phase compensation, the n th channel echo can be expressed as

$$SS_n^{c,p}(f_r, f_a) = W_r(f_r) M_a(f_r) w_a(t_m) \exp \left[-j2\pi \frac{(f_c + f_r)}{c} \cdot \left(\left(-\sin \theta_T - \sin \theta_r - \frac{\varphi_c}{V_c} \right) x_i \right) \right] \exp \left(-j2\pi \frac{(f_c + f_r)}{c} \cdot \left(k_T \left(\frac{x_i}{V_T} \right)^2 + k_r \left(\frac{x_i}{V_r} \right)^2 \right) \right) \sin c \left(f_a + \frac{2(f_c + f_r)}{c} \left(\frac{k_T}{V_T} + \frac{k_r}{V_r} \right) x_i \right). \quad (20)$$

From (20), note that all channel echo is independent of channel baseline after the phase compensation with (19). Then, the vector corresponding to clutter is discussed in Appendix C. An orthogonality vector for the clutter vector is constructed, which is also discussed in Appendix C. With the orthogonality vector, the clutter suppression is implemented. Hence, the residual channel echo after clutter suppression can be expressed as

$$S_{\text{residual}}^{c,p}(f_r, f_a) = SS_1^{c,p}(f_r, f_a) - SS_2^{c,p}(f_r, f_a) = SS_1^c(f_r, f_a) \cdot H_{1,3}(f_r, f_a) - SS_2^c(f_r, f_a) \cdot H_{2,3}(f_r, f_a). \quad (21)$$

From (20) and (21), the residual signal of channel echo is only noise after clutter suppression. So far, the clutter suppression based on orthogonality vector has been presented. With the

$$SS_n^{\text{mov}}(f_r, t_m) = W_r(f_r) M_a(f_r) w_a(t_m) \exp \left(-j\pi \frac{f_r^2}{\gamma} \right) \exp \left[-j2\pi \frac{(f_c + f_r)}{c} \cdot \left(v_{r,r} \left(t_m - \frac{x_i}{V_r} \right) + v_{T,r} \left(t_m - \frac{x_i}{V_T} \right) \right) \right] \exp \left[-j2\pi \frac{(f_c + f_r)}{c} \cdot \left(-(\varphi_r^{\text{mov}} + (V_r + v_{a,r}) \sin \theta_r) \left(t_m - \frac{d_n}{V_r} - \frac{x_i}{V_r} \right) - (V_T + v_{T,a}) \sin \theta_T \left(t_m - \frac{x_i}{V_r} \right) \right) \right] \exp \left[-j2\pi \frac{(f_c + f_r)}{c} \cdot \left(k_{T\text{-mov}} \left(t_m - \frac{x_i}{V_T} \right)^2 + k_{r\text{-mov}} \left(t_m - \frac{d_n}{V_r} - \frac{x_i}{V_r} \right)^2 \right) \right] \quad (13)$$

$$SS_n^c(f_r, t_m) = W_r(f_r) M_a(f_r) w_a(t_m) \exp \left[-j2\pi \frac{(f_c + f_r)}{c} \cdot \left(\left(-\sin \theta_T - \sin \theta_r - \frac{\varphi_c}{V_c} \right) x_i \right) \right] \exp \left[-j2\pi \frac{(f_c + f_r)}{c} \cdot \left(k_T \left(t_m - \frac{x_i}{V_T} \right)^2 + k_r \left(t_m - \frac{d_n}{V_r} - \frac{x_i}{V_r} \right)^2 \right) \right]. \quad (16)$$

$$SS_n^c(f_r, f_a) = W_r(f_r) M_a(f_r) W_a(f_a) \exp \left[-j2\pi \frac{(f_c + f_r)}{c} \cdot \left(\left(-\sin \theta_T - \sin \theta_r - \frac{\varphi_c}{V_c} \right) x_i \right) \right] \exp \left(-j2\pi \frac{(f_c + f_r)}{c} \cdot \left(k_T \left(\frac{x_i}{V_T} \right)^2 + k_r \left(\frac{x_i}{V_r} \right)^2 \right) \right) \sin c \left(f_a + \frac{2(f_c + f_r)}{c} \left(\frac{k_T}{V_T} + \frac{k_r}{V_r} \right) x_i \right) \cdot \exp \left(-j2\pi f_a \eta_c \cdot \left(\frac{d_n}{V_r} \right) \right) \quad (18)$$

proposed clutter suppression approach, the limit of the proposed GEO-LEO bistatic SAR-GMTI system is discussed in Appendix D.

B. Signal Model of the Moving Target After Clutter Suppression

After the RCMC and range compression with (15), the signal of the moving target can be described as (22) as shown at the bottom of this page. where $\theta_{\text{mov}} = (\varphi_r^{\text{mov}} + (V_r + v_{a,r}) \sin \theta_r) \left(\frac{x_i}{V_r}\right) + (V_T + v_{T,a}) \sin \theta_T \left(\frac{x_i}{V_T}\right)$. With the chirp Fourier transform function shown in (17), the signal of moving target after chirp Fourier transform (23) at the bottom, where $\phi_{\text{mov}} = \varphi_r^{\text{mov}} - \varphi_c + v_{a,r} \sin \theta_r + v_{T,a} \sin \theta_T$. During the clutter suppression, the residual signal of the moving target can be

expressed as (24), where $SS_0(f_r, f_a)$ can be expressed as (25) at the bottom.

An approximate expression is adopted, which is shown in

$$\exp \left[j2\pi \frac{(f_c + f_r)}{c} \cdot \left(\frac{d_n}{V_r} \right) (\eta_c \cdot \phi_{\text{mov}} - (\varphi_r^{\text{mov}} - \varphi_c + v_{a,r} \sin \theta_r)) \right] \approx 1. \quad (26)$$

For (26), the low squint mode is considered.

IV. IMAGING PROCESSING FOR THE MOVING TARGET

After the clutter suppression, the constant false alarm (CFAR) technique is utilized to detect the moving target and extract

$$\begin{aligned} SS_n^{\text{mov}}(f_r, t_m) &= W_r(f_r) M_a(f_r) w_a(t_m) \\ &\exp \left[-j2\pi \frac{(f_c + f_r)}{c} \cdot \left(\theta_{\text{mov}} + v_{r,r} \left(t_m - \frac{x_i}{V_r} \right) + v_{T,r} \left(t_m - \frac{x_i}{V_T} \right) \right) \right] \\ &\exp \left[j2\pi \frac{(f_c + f_r)}{c} \cdot \left((\varphi_r^{\text{mov}} - \varphi_c + v_{a,r} \sin \theta_r) \cdot \left(t_m - \frac{d_n}{V_r} \right) + v_{T,a} \sin \theta_T \cdot t_m \right) \right] \\ &\exp \left[-j2\pi \frac{(f_c + f_r)}{c} \cdot \left(k_{T\text{-mov}} \left(t_m - \frac{x_i}{V_T} \right)^2 + k_{r\text{-mov}} \left(t_m - \frac{d_n}{V_r} - \frac{x_i}{V_r} \right)^2 \right) \right] \end{aligned} \quad (22)$$

$$\begin{aligned} SS_n^{\text{mov}}(f_r, f_a) &= W_r(f_r) M_a(f_r) W_a(f_a) \\ &\cdot \exp \left(-j2\pi f_a \eta_c \cdot \left(\frac{d_n}{V_r} \right) \right) \exp \left[-j2\pi \frac{(f_c + f_r) \cdot (v_{r,r} + v_{T,r})}{c} \cdot \eta_c \cdot \left(\frac{d_n}{V_r} \right) \right] \\ &\exp \left(-j2\pi \frac{(f_c + f_r)}{c} \left(\theta_{\text{mov}} + k_T \left(\frac{x_i}{V_T} \right)^2 + k_r \left(\frac{x_i}{V_r} \right)^2 - v_{r,r} \frac{x_i}{V_r} - v_{T,r} \frac{x_i}{V_T} \right) \right) \\ &\exp \left[j2\pi \frac{(f_c + f_r)}{c} \cdot \left(\frac{d_n}{V_r} \right) (\eta_c \phi_{\text{mov}} - (\varphi_r^{\text{mov}} - \varphi_c + v_{a,r} \sin \theta_r)) \right] \\ &\sin c \left(f_a + \frac{(f_c + f_r)}{c} (\eta_c x_i + \phi_{\text{mov}} - (v_{r,r} + v_{T,r})) \right) \end{aligned} \quad (23)$$

$$\begin{aligned} S_{\text{residual}}^{\text{mov}}(f_r, f_a) &= SS_1^{\text{mov}}(f_r, f_a) \cdot H_{1,3}(f_r, f_a) - SS_2^{\text{mov}}(f_r, f_a) \cdot H_{2,3}(f_r, f_a) \\ &\approx \left\{ 1 - \exp \left[-j2\pi \frac{(f_c + f_r) \cdot (v_{r,r} + v_{T,r})}{c} \cdot \eta_c \cdot \left(\frac{d_n}{V_r} \right) \right] \right\} \cdot SS_0(f_r, f_a) \end{aligned} \quad (24)$$

$$\begin{aligned} SS_0(f_r, f_a) &= W_r(f_r) W_a(f_a) M_a(f_r) \\ &\exp \left[j2\pi \frac{(f_c + f_r)}{c} \cdot \left(v_{r,r} \frac{x_i}{V_r} + v_{T,r} \frac{x_i}{V_T} \right) \right] \cdot \exp \left(-j2\pi f_a \cdot \left(\frac{d_n}{V_r} \right) \right) \\ &\exp \left(-j2\pi \frac{(f_c + f_r)}{c} \left(\theta_{\text{mov}} + k_T \left(\frac{x_i}{V_T} \right)^2 + k_r \left(\frac{x_i}{V_r} \right)^2 \right) \right) \\ &\sin c \left(f_a + \frac{(f_c + f_r)}{c} (\eta_c x_i + \phi_{\text{mov}} - (v_{r,r} + v_{T,r})) \right). \end{aligned} \quad (25)$$

the corresponding signal. Then, with the azimuth inverse chirp Fourier transform and inverse RCMC operation, the obtained echo of moving target (27) at the bottom of this page.

The Doppler centroid for the signal shown in (27) can be described as

$$f_{dc} = \frac{f_c \cdot [(\varphi_r^{\text{mov}} + (V_r + v_{a,r}) \sin \theta_r) + (V_T + v_{T,a}) \sin \theta_T]}{c} - \frac{f_c \cdot (v_{r,r} + v_{T,r})}{c}. \quad (28)$$

Inspired by the Doppler centroid estimation approach proposed in [20]–[23], the moving target signal shown in (27) is divided into two parts along the range frequency, which are expressed as $S^{\text{mov}}(f_r - \frac{B_a}{4}, t_m)$ and $S^{\text{mov}}(f_r + \frac{B_a}{4}, t_m)$. B_a denotes the bandwidth of transmitted signal. The corresponding baseband Doppler centroid can be estimated by

$$\begin{aligned} \hat{f}_{dc_baseband_1} &= \frac{PRF}{2\pi} \arg \left\{ E \left[\cdot \text{conj} \left[S^{\text{mov}} \left(f_r - \frac{B_a}{4}, t_m \right) \right] \right] \right\} \\ &= \frac{PRF}{2\pi} \arg \left\{ E \left[\cdot \text{conj} \left[S^{\text{mov}} \left(f_r - \frac{B_a}{4}, t_{m-1} \right) \right] \right] \right\} \end{aligned} \quad (29.a)$$

and

$$\begin{aligned} \hat{f}_{dc_baseband_2} &= \frac{PRF}{2\pi} \arg \left\{ E \left[\cdot \text{conj} \left[S^{\text{mov}} \left(f_r + \frac{B_a}{4}, t_m \right) \right] \right] \right\} \\ &= \frac{PRF}{2\pi} \arg \left\{ E \left[\cdot \text{conj} \left[S^{\text{mov}} \left(f_r + \frac{B_a}{4}, t_{m-1} \right) \right] \right] \right\} \end{aligned} \quad (29.b)$$

where PRF denotes the pulse repetition frequency, $\arg[\cdot]$ is the operation for phase extraction, $\text{conj}[\cdot]$ is the operation for conjugate operation, $E[\cdot]$ is the expectation operation. Then, the coarse estimation of Doppler centroid is

$$\hat{f}_{dc_coarse} = \frac{2f_c}{B_a} (\hat{f}_{dc_baseband_2} - \hat{f}_{dc_baseband_1}). \quad (30)$$

The exact estimation of Doppler centroid is

$$\begin{aligned} \hat{f}_{dc} &= \frac{1}{2} (\hat{f}_{dc_baseband_2} + \hat{f}_{dc_baseband_1}) \\ &+ \text{round} \left(\frac{\hat{f}_{dc_coarse}}{PRF} \right) \cdot PRF \end{aligned} \quad (31)$$

which corresponds to carrier frequency. In (31), $\text{round}[\cdot]$ denotes the integer expectation operation. Then, the linear RCMC function can be expressed as

$$H_1^{\text{mov}}(f_r, t_m) = \exp \left(j2\pi \frac{\hat{f}_{dc}}{f_c} \cdot (f_c + f_r) t_m \right). \quad (32)$$

After the linear RCMC with (32), the echo of the moving target can (33) at the bottom of this page.

Then, the Doppler chirp rate for the moving target signal shown in (33) can be described as

$$k_a = -\frac{f_c}{c} \cdot \left(\frac{(V_T + v_{T,a})^2 \cos^2 \theta_T}{R_T} + \frac{(V_r + v_{a,r})^2 \cos^2 \theta_r}{R_r} \right). \quad (34)$$

The estimated Doppler chirp rate of the moving target is \hat{k}_a using the minimum entropy approach proposed in [24], [25]. Then, the azimuth chirp Fourier transform function can be presented as follows:

$$H_1^{\text{mov}}(f_r, t_m) = \exp \left(j\pi \frac{\hat{k}_a}{f_c} \cdot (f_c + f_r) t_m^2 \right). \quad (35)$$

For the moving target, the azimuth deramp operation in range frequency domain is implemented with (35) and the corresponding signal can be expressed as

$$\begin{aligned} S^{\text{mov}}(f_r, t_m) &= W_r(f_r) M_a(f_r) w_a(t_m) \\ &\exp \left[-j2\pi \frac{(f_c + f_r)}{c} \cdot \left(\theta_{\text{mov}} - \frac{v_{r,r} \cdot x_i}{V_r} - \frac{v_{T,r} \cdot x_i}{V_T} \right) \right] \end{aligned}$$

$$\begin{aligned} S^{\text{mov}}(f_r, t_m) &= W_r(f_r) M_a(f_r) w_a(t_m) \\ &\exp \left[-j2\pi \frac{(f_c + f_r)}{c} \cdot \left(v_{r,r} \left(t_m - \frac{x_i}{V_r} \right) + v_{T,r} \left(t_m - \frac{x_i}{V_T} \right) \right) \right] \\ &\exp \left[-j2\pi \frac{(f_c + f_r)}{c} \cdot \left(-(\varphi_r^{\text{mov}} + (V_r + v_{a,r}) \sin \theta_r) \left(t_m - \frac{x_i}{V_r} \right) - (V_T + v_{T,a}) \sin \theta_T \left(t_m - \frac{x_i}{V_T} \right) \right) \right] \\ &\exp \left[-j2\pi \frac{(f_c + f_r)}{c} \cdot \left(k_{T_mov} \left(t_m - \frac{x_i}{V_T} \right)^2 + k_{r_mov} \left(t_m - \frac{x_i}{V_r} \right)^2 \right) \right]. \end{aligned} \quad (27)$$

$$\begin{aligned} S^{\text{mov}}(f_r, t_m) &= W_r(f_r) M_a(f_r) w_a(t_m) \\ &\exp \left[-j2\pi \frac{(f_c + f_r)}{c} \cdot \left((\varphi_r^{\text{mov}} + (V_r + v_{a,r}) \sin \theta_r) \frac{x_i}{V_r} + (V_T + v_{T,a}) \sin \theta_T \frac{x_i}{V_r} - \frac{v_{r,r} \cdot x_i}{V_r} - \frac{v_{T,r} \cdot x_i}{V_T} \right) \right] \\ &\exp \left[-j2\pi \frac{(f_c + f_r)}{c} \cdot \left(k_{T_mov} \left(t_m - \frac{x_i}{V_T} \right)^2 + k_{r_mov} \left(t_m - \frac{x_i}{V_r} \right)^2 \right) \right]. \end{aligned} \quad (33)$$

$$\exp \left[-j2\pi \frac{(f_c + f_r)}{c} \cdot \left(k_{T_mov} \left(\frac{x_i}{V_T} \right)^2 + k_{r_mov} \left(\frac{x_i}{V_r} \right)^2 \right) \right]$$

$$\exp \left[j2\pi \frac{(f_c + f_r)}{c} \cdot t_m x_i \left(\frac{k_{T_mov}}{V_T} + \frac{k_{r_mov}}{V_r} \right) \right]. \quad (36)$$

Note that there is LRCM brought by the azimuth position. In order to correct the LRCM, the one-step keystone transform is adapted, which is shown as follows [26], [27]:

$$f_c \cdot \tau_m = (f_c + f_r) t_m. \quad (37)$$

After the keystone transform, the signal of moving target can be denoted as

$$S^{\text{mov}}(f_r, \tau_m) = W_r(f_r) M_a(f_r) w_a(\tau_m)$$

$$\exp \left[-j2\pi \frac{(f_c + f_r)}{c} \cdot \left(\theta_{\text{mov}} - \frac{v_{r,r} \cdot x_i}{V_r} - \frac{v_{T,r} \cdot x_i}{V_T} \right) \right]$$

$$\exp \left[-j2\pi \frac{(f_c + f_r)}{c} \cdot \left(k_{T_mov} \left(\frac{x_i}{V_T} \right)^2 + k_{r_mov} \left(\frac{x_i}{V_r} \right)^2 \right) \right]$$

$$\exp \left[j2\pi \frac{(f_c + f_r)}{c} \cdot \tau_m x_i \left(\frac{k_{T_mov}}{V_T} + \frac{k_{r_mov}}{V_r} \right) \right]. \quad (38)$$

After range inverse Fourier transform and azimuth Fourier transform, the focused moving target image can be denoted as where

$$\phi_{\text{mov}} = \theta_{\text{mov}} - \frac{v_{r,r} \cdot x_i}{V_r} - \frac{v_{T,r} \cdot x_i}{V_T} \quad (40)$$

f'_a corresponds the Fourier frequency of τ_m , A_r and A_a are the gain amplitude after range compression and azimuth compression, respectively.

Fig. 2 presents the clutter suppression and moving target imaging processing flowchart. Note that the azimuth baseline for the GEO-LEO MC-SAR-GMTI system echo is range-variant. Then, the range compression, LRCM correction and azimuth chirp Fourier transform are employed to correct the range-variant baseline. After that, azimuth phase compensation and clutter suppression are implemented. After clutter suppression, the moving target signal can be extracted. The LRCM is corrected for the moving target. After the azimuth deramp operations in range frequency domain and keystone transform, the focused moving target image can be obtained.

V. EXPERIMENTS AND DISCUSSIONS

In this section, some simulation experiments are performed to verify the proposed clutter suppression approaches, where

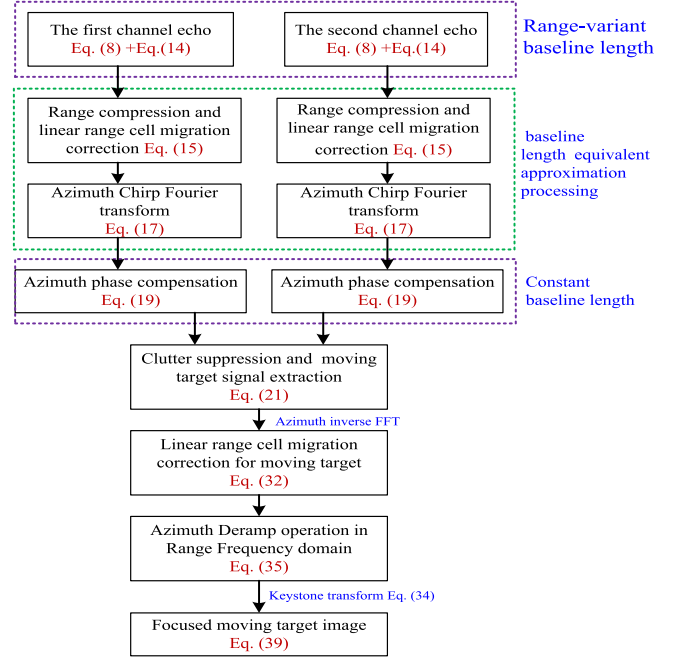


Fig. 2. Clutter suppression and moving target imaging flowchart.

those for clutter suppression and those for fast moving targets are included. More importantly, an experiment with real SAR scattering scene is involved. In addition, the discussions for blind velocity targets are presented.

A. Experiments for Clutter Suppression

1) *Data Description*: A multipoint-target clutter simulation is implemented and the data is collected by a GEO-LEO MC-SAR-GMTI system, where the GEO platform radar is employed to transmit the X-band chirp signal and the LEO platform radar with multichannel antenna is utilized to receive the scene echo. The main system parameters of the GEO-LEO MC-SAR-GMTI system are tabulated in Table I, where the double antennas are distributed along the track of the LEO platform and the corresponding azimuth offset is 5.9 m. During the simulation, the distributing of the clutter scene is shown in Fig. 3(a), where nine-point-targets are involved. Assume that the track of LEO platform and GEO platform is parallel for the data collecting. In addition, there is a moving target with a velocity of 15m/s, whose coordinate is (0, 0).

2) *Results and Experiments' Analysis*: The collected echo by the multichannel GEO-LEO SAR system is presented in

$$S^{\text{mov}}(\hat{t}, f'_a) =$$

$$A_r \sin c \left\{ \hat{t} - \frac{1}{c} \left[\left(R_T + R_r + \Delta R_r^{\text{mov}} \right) + \phi_{\text{mov}} \left(k_{T_mov} \left(\frac{x_i}{V_T} \right)^2 + k_{r_mov} \left(\frac{x_i}{V_r} \right)^2 \right) \right] \right\}$$

$$A_a \sin c \left\{ f'_a - \frac{f_c}{c} \left[\left(R_T + R_r + \Delta R_r^{\text{mov}} \right) + \phi_{\text{mov}} \cdot \left(\frac{x_i \cdot k_{T_mov}}{V_T} \left(\frac{x_i}{V_T} - 1 \right) + \frac{x_i \cdot k_{r_mov}}{V_r} \left(\frac{x_i}{V_r} - 1 \right) \right) \right] \right\} \quad (39)$$

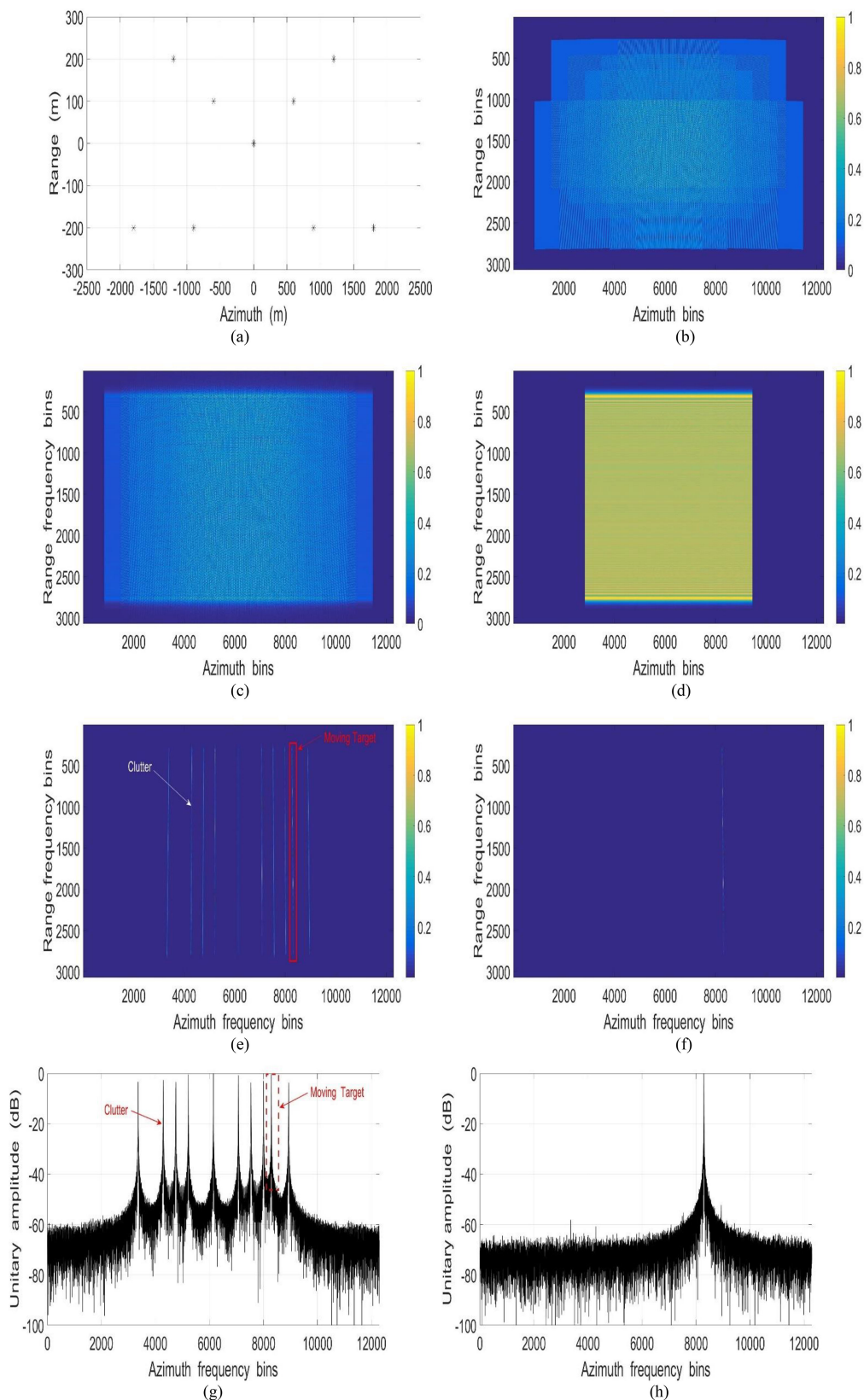


Fig. 3. Clutter suppression processing. (a) Distributing of the clutter scene. (b) Collected echo by the multichannel GE-LEO SAR system. (c) Collected echo in range frequency and azimuth time domain. (d) Moving target echo after clutter suppression in range frequency and azimuth time domain. (e) Collected echo in range frequency and azimuth chirp Fourier transform domain. (f) Moving target echo after clutter suppression in range frequency and azimuth chirp Fourier transform. (g) Azimuth slice for (e). (h) Azimuth slice for (f).

TABLE I
MAIN SYSTEM PARAMETERS FOR THE GEO-LEO MC-SAR-GMTI SYSTEM

Carrier Frequency	9.7 GHz	Channel Number	2
Available Velocity of GEO SAR	3060m/s	Available Velocity of LEO SAR	7600 m/s
Platform Height of GEO SAR	36122 km	Platform Height of LEO SAR	510 km
Squint Angle of GEO SAR	0.2°	Squint Angle of LEO SAR	0.1°
PRF	2400Hz	Bandwidth of transmitted signal	150MHz

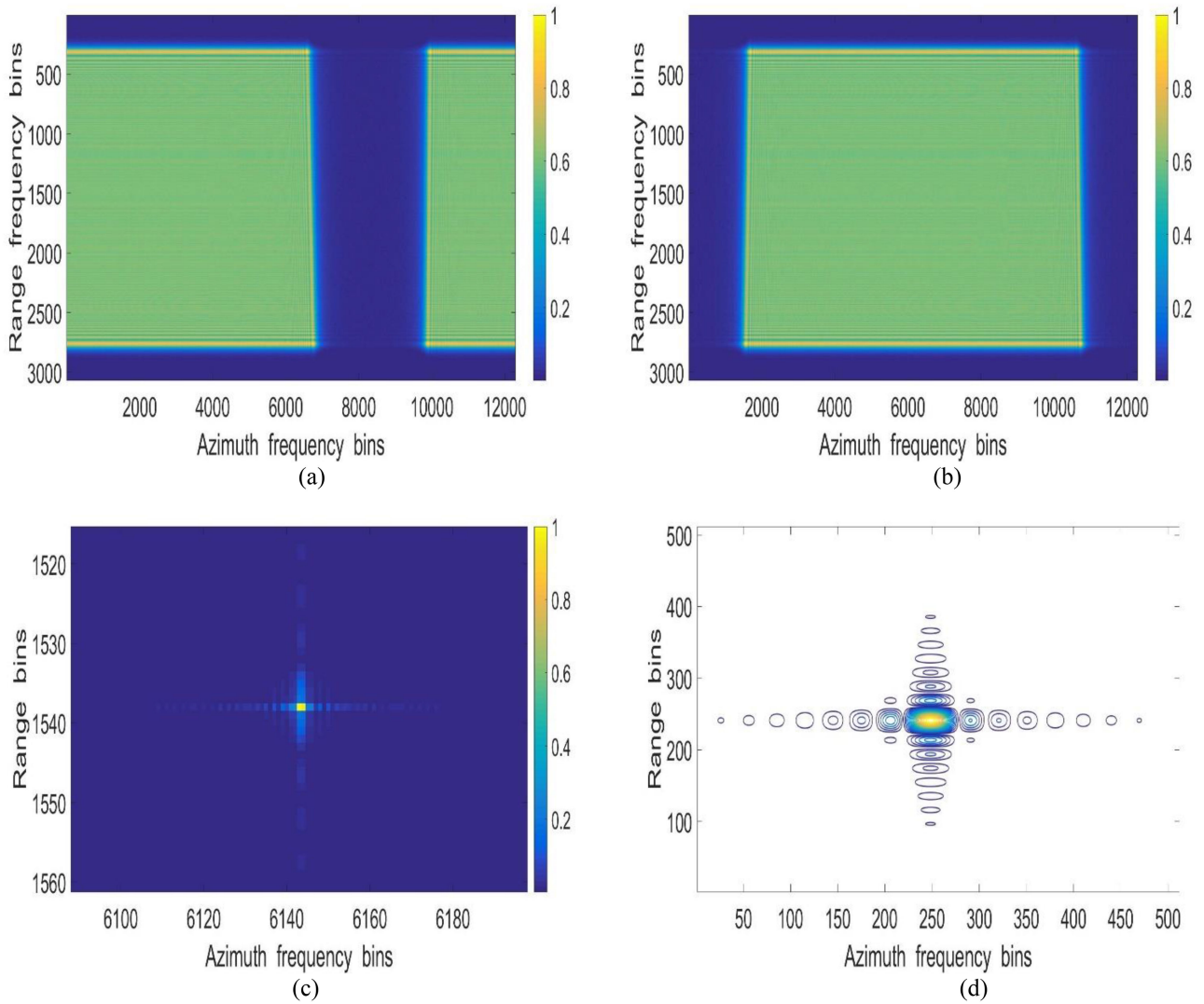


Fig. 4. Moving target imaging processing. (a) Extracted moving target echo in 2-D frequency domain. (b) Moving target echo after the Doppler centroid calibration. (c) Focused moving target image using the proposed imaging processing approach. (d) Focused moving target image after interpolating processing.

Fig. 3(b). After the range Fourier transform, the corresponding echo is shown in Fig. 3(c). Then, the proposed clutter suppression approach is employed to implement the clutter suppression. The extracted moving target echo is shown in Fig, 3(d). In order to further illuminate the clutter suppression process, the collected echo is transformed into the range frequency and azimuth chirp Fourier transform domain, where the phase compensation is implemented. Fig. 3(e) presents the collected echo in range

frequency and azimuth chirp Fourier transform domain, where the clutter and moving target are marked. After the clutter suppression, only the moving target is reserved. Fig. 3(g) and (h) denotes the azimuth slice for the Fig. 3(e) and (f), respectively. Note that the clutter can be suppressed well and the signal of moving target is preserved.

With the extracted the moving target echo shown in Fig. 4(h), the inverse chirp Fourier transform is implemented. The obtained

moving target echo in 2-D frequency is shown in Fig. 4(a), where there is an offset for Doppler spectrum. With the estimated Doppler centroid, the Doppler centroid compensation is achieved and the corresponding 2-D spectrum is given in Fig. 4(b). Then, the proposed moving target imaging algorithm in this article is utilized to focus the moving target. The focused moving target can be obtained and the corresponding result is exhibited in Fig. 4(c). After the 16 times interpolating processing, the focused moving target image is shown in Fig 4(d), where the peak-to-sidelobe ratio (PSLR) in range is -13.26 dB and PSLR in azimuth is -13.23 dB. Hence, the moving target can be well focused.

B. Experiments for Fast Moving Targets

In order to discuss the clutter suppression and image processing for the fast moving targets, another simulation experiment is implemented. The system parameters and clutter scene shown in Part A in this section are involved. For the fast moving targets in the imaging scene, the Doppler centroid brought by the slant-velocity is ambiguous. The proposed baseband Doppler centroid estimation algorithm in [19] can be utilized to estimate the baseband component of Doppler centroid. Then, the Doppler centroid ambiguity number estimation approach proposed in [20] is employed to obtain the Doppler centroid ambiguity number for the moving target. Compared to the slow moving target with an unambiguous Doppler centroid, the Doppler centroid ambiguity number estimation is very important. During this experiment, the moving target with an along y -axis velocity of 50 m/s is involved, where the Doppler centroid ambiguity number is 1. After the clutter suppression, the extracted fast moving target echo in range frequency and azimuth chirp Fourier transform domain is given in Fig. 5(a). Compared to the slow target shown in Fig. 3(f), the fast moving target has more obvious slope. After azimuth inverse chirp Fourier transform, the reconstructed fast moving target echo in 2-D frequency domain is presented in Fig. 5(b). With the estimated baseband component of Doppler centroid, the Doppler centroid compensation is implemented and the corresponding echo in 2-D frequency domain is shown in Fig. 5(c). Note that the 2-D frequency spectrum of moving target has a slope. After the range cell migration correction, the moving target in 2-D time domain is given in Fig. 5(d). One can note that the signal of moving target is not aligned along azimuth, which means the energy of moving target dispersing some range bins. After the image processing, the moving target cannot be well focused, which is shown Fig. 5(e).

The Doppler centroid ambiguity number estimation algorithm is employed to estimate Doppler centroid ambiguity number and the corresponding estimation value is 1. With the estimated accurate Doppler centroid, the moving target echo after Doppler centroid compensation is shown in Fig. 6(a). After the range compression, the corresponding signal is presented in Fig. 6(b). Then, after the range cell migration correction, the moving target signal is aligned along the azimuth. The well-focused moving target is presented in Fig. 6(d). After the interpolating processing, the corresponding moving target image is shown in Fig. 6(e).

Note that the performance of the proposed clutter suppression and moving target imaging is well for the fast moving target.

C. Simulation Experiment With Real SAR Scene

In order to further discuss the performance of the proposed clutter suppression approach, a simulation experiment with real SAR scattering scene is implemented. The system parameters are shown in Table I and the real SAR scene is shown in Fig. 7(a). During the simulation experiment, the complex SAR image of real scene is used as the scattering coefficient to simulate the clutter, where a triple trunk road, some building, overpasses, playground, etc., are involved. At the same time, a moving target with a velocity of 37 m/s is involved, which is located on the main road. To analyze the performance of clutter suppression, the scattering coefficient of moving target is below the clutter. Fig. 7(b) presents the simulated clutter and moving target in range frequency and azimuth time domain. Note that the moving target echo is lost in the clutter. After the azimuth chirp Fourier transform processing, the signal of moving target and clutter are both cumulated in azimuth. The corresponding result is shown in Fig. 7(d). The signal of moving target is marked by red rectangle window. It can be seen that there is some clutter with higher amplitude than the moving target. If the constant CFAR detection technique is utilized to detect the moving target, a very high false alarm ratio is unavioded. An azimuth slice corresponding to the signal marked by the white line in Fig. 7(d) is shown in Fig. 7(f). For the signal of the azimuth slice, the moving target is submerged by the clutter.

After the clutter suppression with the proposed clutter suppression approach in this article, the corresponding result is presented in Fig. 7(c). Compared to Fig. 7(b), the clutter is well suppressed. Fig. 7(e) displays the signal of moving target after the azimuth chirp Fourier transform, which is corresponding to the echo shown in Fig. 7(d) after clutter suppression. Note that the signal of moving target is prominent, and the background is very faint. After the clutter suppression processing, the signal shown in Fig. 7(f) is displayed in Fig. 7(g). The signal of moving target is accentuated from the noise. Compared to Fig. 7(f), it illuminates the well performance of the proposed clutter suppression approach.

D. Discussions for Blind Velocity

From (24), when the moving target has some given slant-velocities, i.e., (38) is established, the moving target echo is completely suppressed during the clutter suppression. These given slant-velocities are called blind velocity

$$\left\{ 1 - \exp \left[\frac{-j2\pi \frac{(f_c + f_r) \cdot (v_{r,r} + v_{T,r})}{c}}{\frac{V_r \cos^2 \theta_r}{R_r}} \cdot \left(\frac{d_n}{V_r} \right) \right] \right\} \approx 0. \quad (38)$$

From (38), one can have

$$v_{r,r} + v_{T,r} = i \cdot \frac{\left(\frac{V_T \cos^2 \theta_T}{R_T} + \frac{V_r \cos^2 \theta_r}{R_r} \right)}{\frac{V_r \cos^2 \theta_r}{R_r}} \cdot \left(\frac{V_r}{d_n} \right) \cdot \frac{c}{(f_c + f_r)} \quad (39)$$

$i = \dots - 2, -1, 0, 1, 2 \dots$

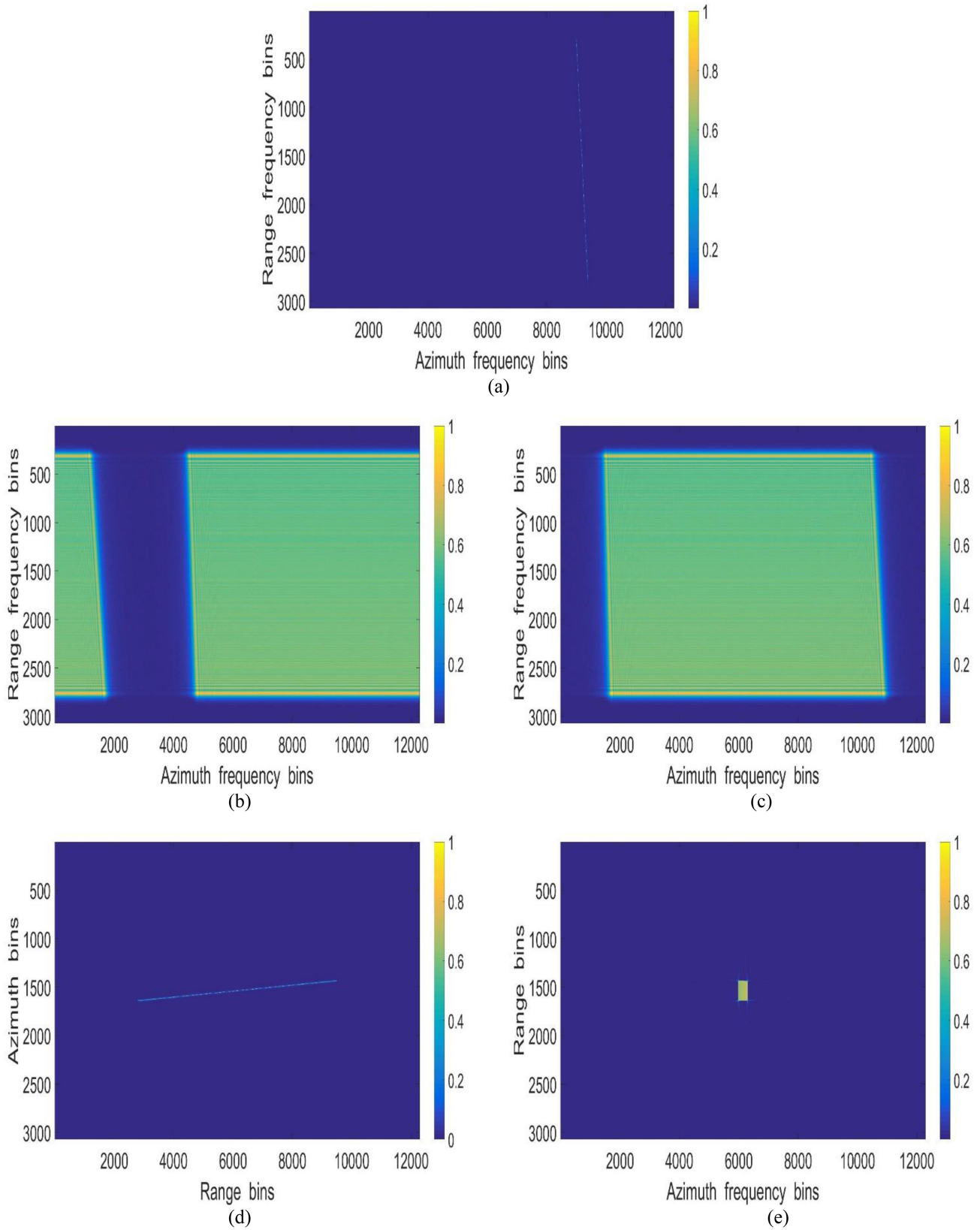


Fig. 5. Fast moving target imaging processing with mismatch Doppler centroid. (a) Extracted moving target echo in range frequency and azimuth chirp Fourier transform domain. (b) Reconstructed moving target echo in 2-D frequency domain. (c) Moving target echo in 2-D frequency domain after mismatch Doppler centroid compensation. (d) Moving target signal in 2-D time domain after range compression and range cell migration correction. (e) Image result for the moving target.

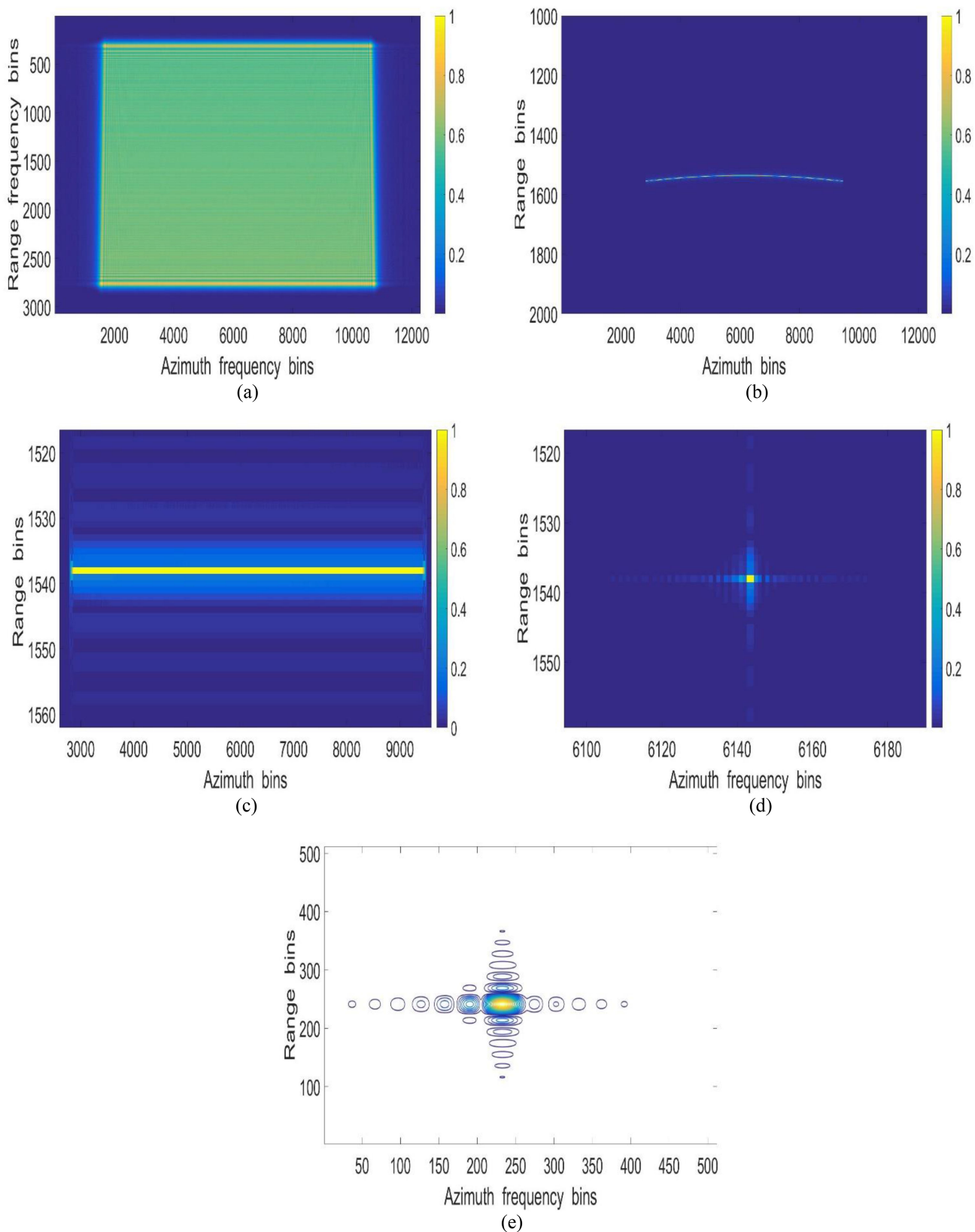


Fig. 6. Fast moving target imaging processing with accurate Doppler centroid. (a) Reconstructed moving target echo in 2-D frequency domain after the accurate Doppler centroid compensation. (b) Moving target echo after range compensation. (c) Moving target echo after range cell migration correction. (d) Focused moving target image. (e) Focused moving target image after interpolating processing.

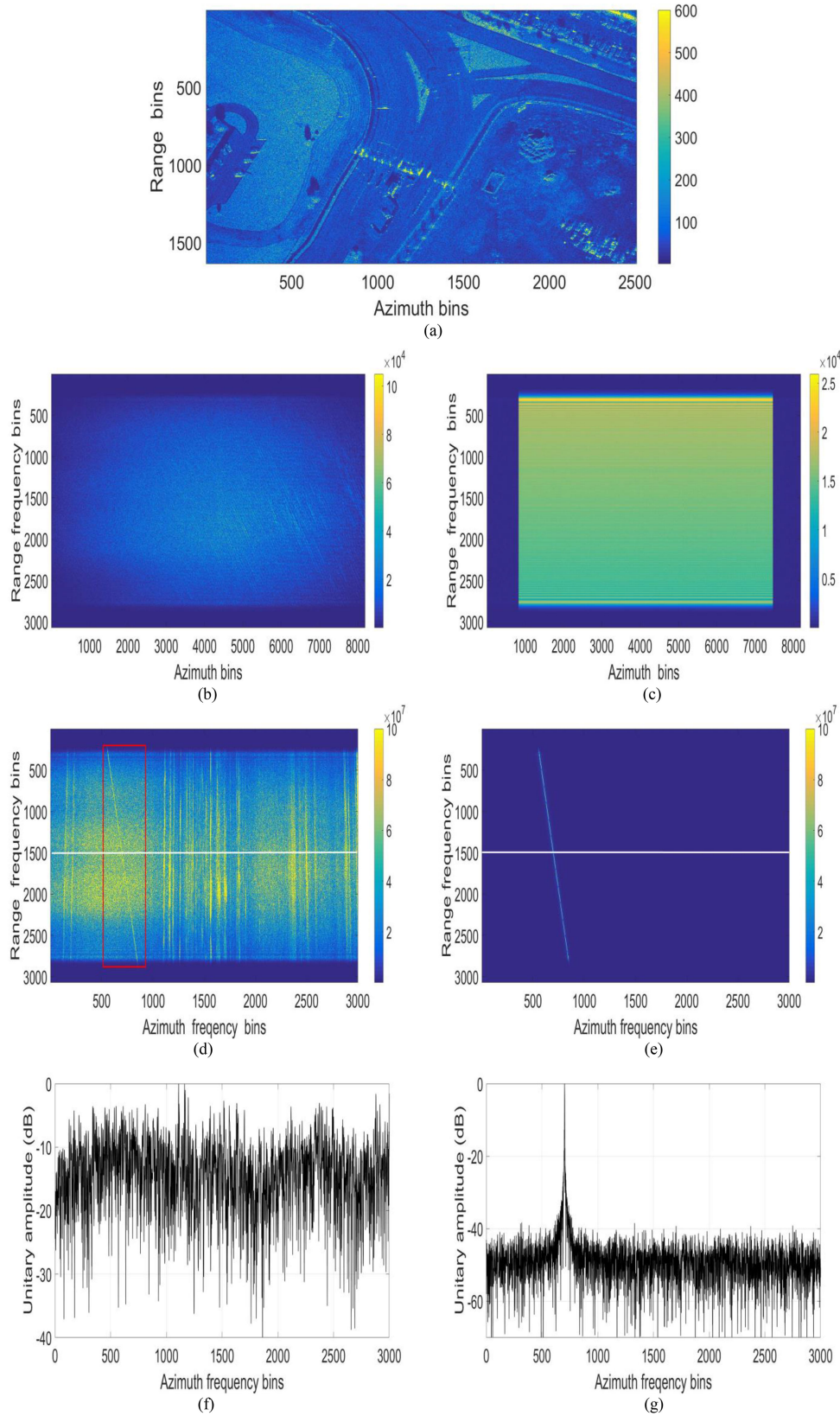


Fig. 7. Simulation experiment with real SAR scene. (a) Complex SAR image of real scene. (b) Simulated GEO-LEO bistatic SAR-GMTI echo. (c) Echo after clutter suppression. (d) Simulated GEO-LEO bistatic SAR-GMTI echo in range frequency and azimuth CFT domain. (e) Simulated GEO-LEO bistatic SAR-GMTI echo after clutter suppression in range frequency and azimuth CFT domain. (f) Signal corresponding to the signal marked by the white line in Fig. 6(d). (g) Signal corresponding to the signal marked by the white line in Fig. 6(e).

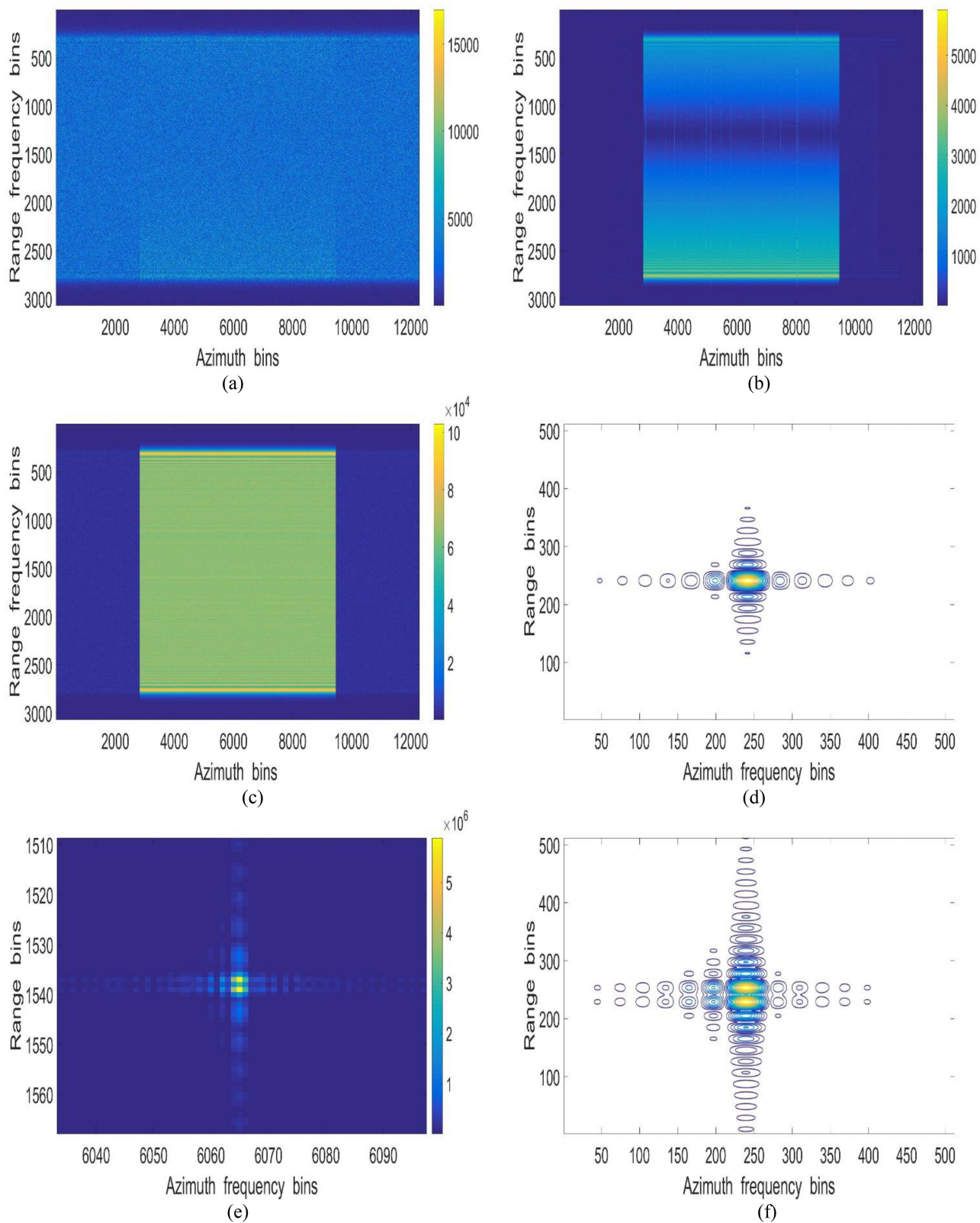


Fig. 8. Discussion for the blind velocity. (a) Moving target echo with a velocity of 40.18 m/s and 0 dB noise after clutter suppression. (b) Moving target echo with a velocity of 40.18 m/s and 40 dB noise after clutter suppression. (c) Moving target echo with a velocity of 20 m/s and 0 dB noise after clutter suppression. (d) Image result for the moving target echo with a velocity of 20 m/s and 0 dB noise. (e) Image result for the moving target echo with a velocity of 40.18 m/s and 40 dB noise. (f) Image result corresponding to (e) after interpolating processing.

where c denotes integer. The corresponding velocity value for $v_{r,r}+v_{T,r}$ is blind velocity. In order to further discuss the blind velocity for the moving target, some experiments are implemented, where the system parameters are as same as Section V-A. When the moving target has a velocity along y -axis of 40.18 m/s, the corresponding slant-velocity of $v_{r,r}+v_{T,r}$ is in the region of blind velocity. When the noise of the clutter and moving target echo is 0 dB, the moving target signal after clutter suppression is shown in Fig. 8(a). Note that moving target echo is covered with noise. When the noise of the clutter and moving target echo is 40 dB, the moving target signal after clutter suppression is presented in Fig. 8(b). Note that some frequency spectrum signal is completely suppressed while the other has obviously energy loss. When the moving target has a velocity along y -axis of 20 m/s, the corresponding slant-velocity of $v_{r,r}+v_{T,r}$ is not in the region of blind velocity. The extracted moving target echo is shown in Fig. 8(c) with a trivial energy loss. After the image processing, the corresponding image result is shown Fig. 8(d), where the interpolating processing is involved. We note that the moving target with a velocity along y -axis of 20 m/s can be well focused. When the target moves at a velocity along y -axis of 40.18 m/s, the image result is presented in Fig. 8(e). After the interpolating processing, the corresponding result is shown in Fig. 8(f). Note that the moving target in blind velocity region cannot be focused, i.e., the moving target is split into multipoint target.

VI. CONCLUSION

This article explores the SAR-GMTI capabilities of the GEO-LEO bistatic multichannel SAR system. Considering that the baseline varies with clutter scene in azimuth Doppler Fourier transform domain, the chirp Fourier transform is introduced and the echo in azimuth chirp Fourier transform domain is analyzed. With the approximation processing, the baseline is invariant with clutter scene, where a linear phase is displayed for different channel echo. Then, the baseline compensation is implemented for the clutter in the observation scene. Comparing the clutter signal and moving target signal, the clutter is suppressed in range frequency and azimuth chirp Fourier transform domain and the moving target echo is extracted. For the moving target imaging processing, three-step operation is involved, i.e., the Doppler centroid correction, azimuth chirp Fourier transform, and one-step keystone. During the Doppler centroid correction, the Doppler centroid estimation is critical. For the slow moving target, the baseband Doppler centroid estimation is adequate for imaging processing. For fast moving target, the process of Doppler ambiguity number estimation must be included. Finally, some simulation experiments of the GEO-LEO MC-SAR-GMTI data are employed to verify the accuracy and efficiency of our proposed algorithms. At the same time, some details for blind velocity targets are discussed with simulation experiment results.

APPENDIX A

DISCUSSIONS FOR THE GEOMETRY APPROXIMATION

Fig. 9 presents the geometry for the GEO-LEO MC-SAR-GMTI system, where the orbit height of the GEO-SAR platform

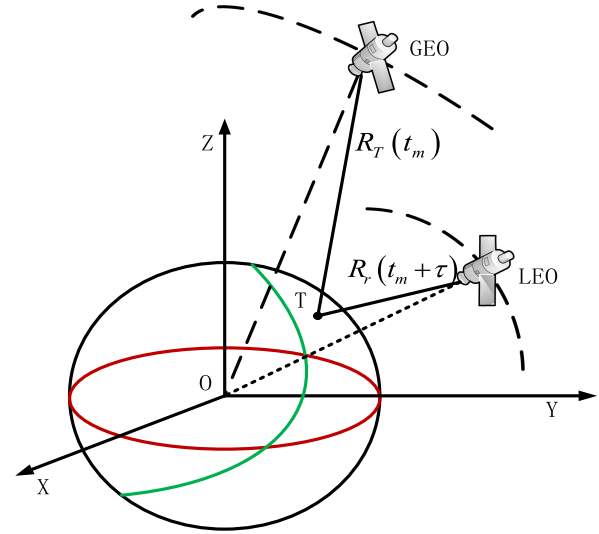


Fig. 9. Geometry for the GEO-LEO MC-SAR-GMTI system.

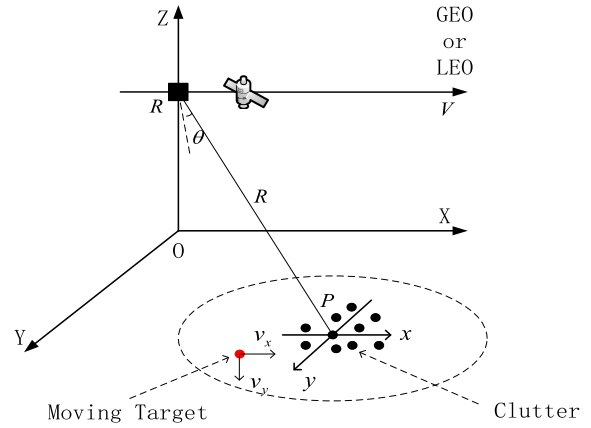


Fig. 10. Approximate geometry model for the GEO platform or LEO platform SAR system.

is 36122 km and the orbit height of the LEO-SAR platform is 510 km (taking the simulation parameter as an example). The radius of earth is about 6371 km, i.e., $R_e = 6371\text{km}$. For a swath of 100 km, i.e., $L = 100\text{km}$, the swath corresponding to earth center angle is:

$$\phi_{\text{angle}} = \frac{L}{R_e} \cdot \frac{180}{\pi} = \frac{100\text{km}}{6371\text{km}} \cdot \frac{180}{\pi} = 0.899^\circ. \quad (\text{A.1})$$

When the earth center angle is less than 1° , the curve of swath is small enough to be ignored. In this article, the discussed swath is less than 100 km and the curve of swath is neglected. When the resolution is below 1 m, the curve of trajectory can be ignored. For the space-borne SAR-GMTI system, the resolution is usually below 1 m. Hence, the GEO-SAR and LEO-SAR platform can be both approximated as shown in Fig. 10. The differences lie in different velocity, height, squint angle, slant-range, etc. It is worth to point out that Fig. 1 is an approximate model for Fig. 9. The corresponding conditions are that the swath is below 100 km and the resolution is below 1m.

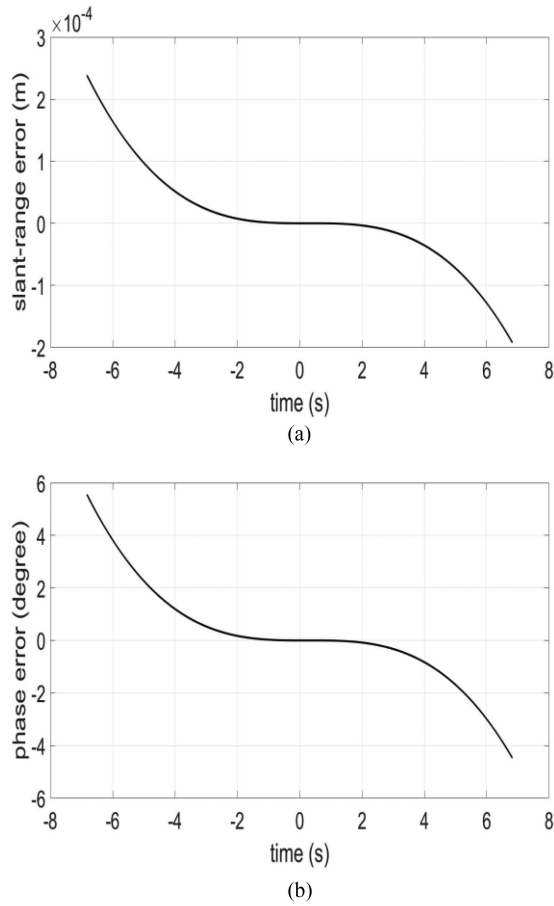


Fig. 11. Approximate error for the slant-range and phase. (a) Approximate error for the slant-range. (b) Approximate error for phase.

APPENDIX B

DISCUSSIONS FOR THE SLANT-RANGE APPROXIMATION

The slant-range of the echo can be expressed as

$$R(t_m) = R_T(t_m) + R_R(t_m + \tau) \quad (\text{B.1})$$

where $R_T(t_m)$ and $R_R(t_m + \tau)$ are expressed by (1) and (3), respectively. $\tau = -\Delta T$ in (3). In order to derivation convenient, $\Delta T \approx \frac{(R_r + R_T)}{c}$ is adopted in (5). The error brought by the approximate processing can be described as

$$\begin{aligned} \Delta R_{\text{error}} = & R_R \left(t_m + \frac{R_T(t_m) + R_R(t_m + \tau)}{c} \right) \\ & - R_R \left(t_m + \frac{R_T + R_r}{c} \right). \end{aligned} \quad (\text{B.2})$$

Fig. 11 presents the approximate error for the slant-range and phase, which can be expressed as

$$\Delta\phi = \frac{4\pi}{\lambda} \cdot \Delta R_{\text{error}} \quad (\text{B.3})$$

Note the order of slant-range error is 10^{-4} , the corresponding phase error is below 10° . When the phase error is below 45° , the

influence for moving target imaging processing can be ignored. Hence, the slant-range approximation in this article is feasible.

APPENDIX C

DISCUSSION FOR CLUTTER SUPPRESSION

After the phase compensation with (19), the echo vector of clutter can be expressed as

$$\begin{bmatrix} 1 \\ 1 \end{bmatrix} \cdot SS_n^{c,p}(f_r, f_a). \quad (\text{C.1})$$

Then, the echo vector of moving target can be described as

$$\begin{bmatrix} 1 \\ \exp(j\phi_{\text{mov}}) \end{bmatrix} \cdot SS_0(f_r, f_a) \quad (\text{C.2})$$

where

$$\begin{aligned} \phi_{\text{mov}} = & -2\pi \cdot \frac{(f_c + f_r)(v_{r,r} + v_{T,r})}{c} \\ & \cdot \frac{\frac{V_r \cos^2 \theta_r}{R_r}}{\frac{V_T \cos^2 \theta_T}{R_T} + \frac{V_r \cos^2 \theta_r}{R_r}} \cdot \frac{d_n}{V_r}. \end{aligned} \quad (\text{C.3})$$

In order to suppress clutter, an orthogonality vector for $\begin{bmatrix} 1 \\ 1 \end{bmatrix}$ can be expressed as $\begin{bmatrix} 1 & -1 \end{bmatrix}$. With the vector of $\begin{bmatrix} 1 & -1 \end{bmatrix}$ for clutter suppression, the clutter suppression can be described as

$$\begin{bmatrix} 1 & -1 \end{bmatrix} \cdot \begin{bmatrix} 1 \\ 1 \end{bmatrix} \cdot SS_n^{c,p}(f_r, f_a). \quad (\text{C.4})$$

The corresponding result can be expressed as (21). After the clutter suppression, the residual signal of moving target can be written as

$$\begin{bmatrix} 1 & -1 \end{bmatrix} \cdot \begin{bmatrix} 1 \\ \exp(j\phi_{\text{mov}}) \end{bmatrix} \cdot SS_0(f_r, f_a). \quad (\text{C.5})$$

The corresponding result can be expressed as (24).

APPENDIX D

DISCUSSIONS FOR THE LIMITS OF THE PROPOSED GEO-LEO MC-SAR-GMTI SYSTEM

In this article, the orthogonality vector of clutter is employed to suppress clutter. In theory, the clutter can be well-suppressed. Hence, after the clutter suppression, the amplitude of clutter is 0 and the influence of clutter can be approximately ignored during the detection of moving target. In addition, since the operation of clutter suppression is linearity, the level of noise stays the same. Assume that the power of noise is 1, i.e., $P_{\text{noise}} = 1$. From (C.2), the vector of moving target is

$$\frac{1}{\sqrt{2}} \cdot \begin{bmatrix} 1 \\ \exp(j\phi_{\text{mov}}) \end{bmatrix} \cdot \sqrt{P_a} \quad (\text{D.1})$$

where ϕ_{mov} is shown in (C.3), and P_a denotes the power of the moving target in the range frequency and azimuth CFT frequency domain for the GEO-LEO bistatic SAR-GMTI system. With the coefficient of $\frac{1}{\sqrt{2}}$, the power of the whole system is P_a for the moving target.

Since the amplitude of clutter is 0, the SNR of moving target is equal to the signal-to-clutter and noise ratio (SCNR). With

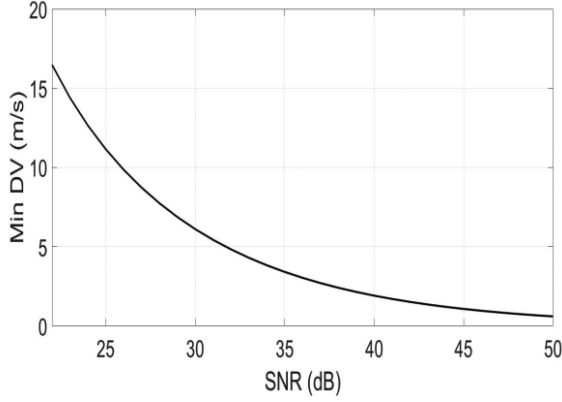


Fig. 12. Relationship between the minimum detectable velocity and SNR.

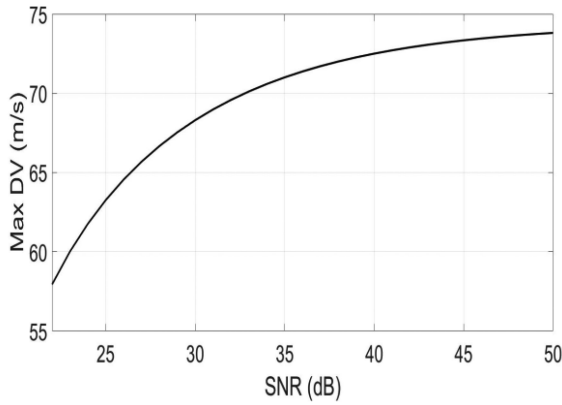


Fig. 13. Relationship between the maximum detectable velocity and SNR.

the vector $[1 \ -1]$ for clutter suppression, the signal of moving target after clutter suppression can be expressed as

$$S_{\text{mov}} = \frac{1}{\sqrt{2}} (1 - \exp(j\phi_{\text{mov}})) \cdot \sqrt{P_a}. \quad (\text{D.2})$$

The total power of the moving target is

$$P_{\text{mov}} = S_{\text{mov}} \cdot \text{conj}(S_{\text{mov}}) = (1 - \cos \phi_{\text{mov}}) \cdot P_a. \quad (\text{D.3})$$

Since the power of noise is 1, the SNR of moving target is

$$\text{SNR}_{\text{mov}} = 10 \log \left(\frac{P_{\text{mov}}}{P_{\text{noise}}} \right) = 10 \log \{ (1 - \cos \phi_{\text{mov}}) \cdot P_a \}. \quad (\text{D.4})$$

Let P_D be the detection probability and P_{FA} be the false alarm probability. Then the SNR is transformed to

$$\text{SNR}_{\text{mov}} = 10 \cdot \log \left(\frac{\log P_{FA}}{\log P_D} - 1 \right). \quad (\text{D.5})$$

With an acceptability detection probability and false alarm probability, i.e., $P_D = 90\%$ and $P_{FA} = 10^{-6}$, the corresponding SNR of moving target is 21.14 dB. With the system parameters shown in simulation experiment, the minimum and maximum detectable speed can be discussed. Fig. 12 presents the relationship between the minimum detectable velocity and the SNR of moving target. Note that the minimum detectable velocity

descends with the ascending of SNR. Fig. 13 presents the relationship between the maximum detectable velocity and the SNR of moving target. Note that the maximum detectable velocity ascends with the increase of SNR. The maximum detectable velocity corresponding to 50 dB is closed to the first blind velocity, which is discussed in Section V-D.

In addition, the proposed clutter suppression approach can work well for the parallel baseline mode, where the squints are both low for SAR-GMTI processing. For the perpendicular baseline mode, it is difficult to keep that the squints are both low for GEO-SAR platform and LEO-SAR platform.

REFERENCES

- [1] C. Diego and W. Ingo, "Joint monostatic and bistatic STAP for improved SAR-GMTI capabilities," *IEEE Trans Geosci. Remote Sens.*, vol. 54, no. 3, pp. 1834–1848, Mar. 2016.
- [2] Y. Liao, J. Qian, L. Yang, and M. Xing, "Space-surface bistatic SAR-GMTI," in *Proc. IEEE CIE Int. Conf. Radar*, Oct. 2011, pp. 903–906.
- [3] Z. Sun, J. Wu, J. Pei, Z. Li, Y. Huang, and J. Yang, "Inclined geosynchronous spaceborne-airborne bistatic SAR: Performance analysis and mission design," *IEEE Trans. Geosci. Remote Sens.*, vol. 54, no. 1, pp. 343–357, Jan. 2016.
- [4] Y. Wang, Y. Liu, Z. Li, Z. Suo, C. Fang, and J. Chen, "High-resolution wide-swath imaging of spaceborne multichannel bistatic SAR with inclined geosynchronous illuminator," *IEEE Geosci. Remote Sens. Lett.*, vol. 14, no. 12, pp. 2380–2384, Dec. 2017.
- [5] P. Huang, X. Xia, G. Liao, Z. Yang, and Y. Zhang, "Long-time coherent integration algorithm for radar maneuvering weak target with acceleration rate," *IEEE Trans. Geosci. Remote Sens.*, vol. 57, no. 6, pp. 3528–3542, Jan. 2019.
- [6] P. Huang, X. Xia, G. Liao, Z. Yang, J. Zhou, and X. Liu, "Ground moving target refocusing in SAR imagery using scaled GHAF," *IEEE Trans. Geosci. Remote Sens.*, vol. 56, no. 2, pp. 1030–1045, Feb. 2018.
- [7] Z. Lv, S. Liu, and Y. Wang, "System design of GEO-LEO bistatic SAR with high-resolution and wide swath," in *Proc. IEEE Int. Conf. Mechatronics, Robot. Autom.*, May 2018, pp. 1–5.
- [8] H. Yan, R. Wang, F. Li, Y. Deng, and Y. Liu, "Ground moving target extraction in a multichannel wide-area surveillance SAR/GMTI system via the relaxed PCP," *IEEE Geosci. Remote Sens. Lett.*, vol. 10, no. 3, pp. 617–621, Jan. 2013.
- [9] K. S. Thomas *et al.* "Suppression of clutter in multichannel SAR GMTI," *IEEE Trans. Geosci. Remote Sens.*, vol. 52, no. 7, pp. 4005–4013, Jul. 2014.
- [10] J. Ward, "Space-time adaptive processing for airborne radar," MIT Lincoln Lab., Lexington, MA, USA, Tech. Rep. 1015, 1994.
- [11] W. L. Melvin, "Space-time adaptive radar performance in heterogeneous clutter," *IEEE Trans. Aerosp. Electron. Syst.*, vol. 36, no. 2, pp. 621–633, Apr. 2000.
- [12] M. Eduardo, V. B. Stefan, J. Marc, and B. Antoni, "Multichannel SAR-GMTI in maritime scenarios with F-SAR and TerraSAR-X sensors," *IEEE J. Sel. Topics Appl. Earth Observ. Remote Sens.*, vol. 8, no. 11, pp. 5052–5076, Nov. 2015.
- [13] W. Q. Wang, "Multichannel SAR using waveform diversity and distinct carrier frequency for ground moving target indication," *IEEE J. Sel. Topics Appl. Earth Observ. Remote Sens.*, vol. 8, no. 11, pp. 5040–5052, Nov. 2015.
- [14] L. Wen, J. Ding, and O. Loffeld, "Video SAR moving target detection using dual faster R-CNN," *IEEE J. Sel. Topics Appl. Earth Observ. Remote Sens.*, vol. 14, pp. 2984–2994, Feb. 25, 2021.
- [15] L. Lightstone, D. Faubert, and G. Rempel, "Multiple phase center DPCA for airborne radar," in *Proc. IEEE Nat. Radar Conf.*, 1991, pp. 36–40.
- [16] C. H. Gierull, "Statistical analysis of multilook SAR interferograms for CFAR detection of ground moving targets," *IEEE Trans. Geosci. Remote Sens.*, vol. 42, no. 4, pp. 691–701, Apr. 2004.
- [17] C. H. Gierull, "Ground moving target parameter estimation for two-channel SAR," *Proc. Inst. Elect. Eng.-Radar Sonar Navigation*, vol. 153, no. 3, pp. 224–233, Jun. 2006.
- [18] S. Axelsson, "Position correction of moving targets in SAR imagery," *Proc. SPIE*, vol. 5236, pp. 80–92, 2004.

- [19] Y. Wang, Y. Liu, Z. Li, Z. Suo, C. Fang, and J. Chen, "High-resolution wide-swath imaging of spaceborne multichannel bistatic SAR with inclined geosynchronous illuminator," *IEEE Geosci. Remote Sens. Lett.*, vol. 14, no. 12, pp. 2380–2384, Dec. 2017.
- [20] I. G. Cumming and F. H. Wong, *Digital Processing of Synthetic Aperture Radar Data: Algorithm and Implementation*. Norwood, MA, USA: Artech House, 2005.
- [21] R. Bamler, "Doppler frequency estimation and the Cramer-Rao bound," *IEEE Trans. Geosci. Remote Sens.*, vol. 29, no. 3, pp. 385–390, May 1991.
- [22] I. G. Cumming and S. Li, "Improved slope estimation for SAR Doppler ambiguity resolution," *IEEE Trans. Geosci. Remote Sens.*, vol. 44, no. 3, pp. 707–718, Mar. 2006.
- [23] Y. Kong, B. Cho, and Y. Kim, "Ambiguity-free Doppler centroid estimation technique for airborne SAR using the radon transform," *IEEE Trans. Geosci. Remote Sens.*, vol. 43, no. 4, pp. 715–721, Apr. 2005.
- [24] L. M. Robert, N. D. Minh, and C. M. David, "SAR image autofocus by sharpness optimization: A theoretical study," *IEEE Trans. Image Process.*, vol. 16, no. 9, pp. 2309–2321, Sep. 2007.
- [25] L. Xi and J. Ni, "Autofocusing of ISAR images based on entropy minimization," *IEEE Trans. Aerosp. Electron. Syst.*, vol. 35, no. 4, pp. 1240–1252, Oct. 1999.
- [26] D. Zhu, Y. Li, and Z. Zhu, "A keystone transform without interpolation for SAR ground moving-target imaging," *IEEE Trans. Geosci. Remote Sens.*, vol. 45, no. 1, pp. 18–22, Jan. 2007.
- [27] P. Huang, X. Xia, X. Liu, and G. Liao, "Refocusing and motion parameter estimation for ground moving targets based on improved axis rotation-time reversal transform," *IEEE Trans. Comput. Imag.*, vol. 4, no. 3, pp. 479–494, Sep. 2018.



Junli Chen was born in 1971. He received the B.S. degree in electrical engineering and automation from the Harbin Institute of Technology, Harbin, China, in 1996, the Ph.D. degree in electrical engineering from Shanghai Jiaotong University, Shanghai, China, in 2010.

His research interests include the system design and signal processing for the spaceborne radar and interferometric SAR systems.

Dr. Chen is currently a member of the Shanghai Academy of Spaceflight Technology, Shanghai, China.



Yanyang Liu was born in 1987. He received the B.S. degree in electrical and information engineering from Xinjiang University, Xinjiang, China, in 2008, the Ph.D. degree in electrical engineering from Xidian University, Xi'an, China, in 2014.

His research interests include the system design and signal processing for the spaceborne synthetic aperture radar (SAR) and interferometric SAR systems.

Dr. Liu is currently a member of the Shanghai Institute of Satellite Engineering, Shanghai, China.

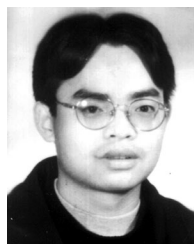


Shuang-Xi Zhang (Member, IEEE) was born in Fujian Province, China, in 1984. He received the B.S. degree in technique of measuring control and instrument engineering from Xidian University, Xian, China, in 2008, and the Ph.D. degree in signal processing from the National Key Lab of Radar Signal Processing, Xidian University in 2014.

He was a Research Fellow with the National University of Singapore (NUS), Singapore, during 2014–2016. He is currently an Associate Professor with the School of Electronics and Information, Northwestern

Polytechnical University, Xi'an, China. His research interests include SAR imaging, clutter suppression, SAR interference suppression, array signal processing, and electromagnetic scattering, etc.

Dr. Zhang is the Organizer and Session Chairs of Synthetic Aperture Radar Techniques and Applications-Part1/2 and -Part2/2 in ACES-China 2017, Suzhou.



Mengdao Xing (Fellow, IEEE) received the B.S. and Ph.D. degrees from Xidian University, Xi'an, China, in 1997 and 2002, respectively.

He is currently a Professor with the National Laboratory of Radar Signal Processing, Xidian University. He holds the appointment of Dean with the Academy of Advanced Interdisciplinary Research Department, Xidian University. He has written or cowritten more than 200 refereed scientific journal papers. He also has authored or coauthored two books about SAR signal processing. The total citation times of his re-

search are greater than 10 000 (H-index 50). He has achieved over 50 authorized China patents. His research has been supported by various funding programs, such as National Science Fund for Distinguished Young Scholars. His current research interests include synthetic aperture radar (SAR), SAR interferometry (InSAR), inverted synthetic aperture radar (ISAR), sparse signal processing, and microwave remote sensing.

Dr. Xing has held several special issues on IEEE GRSM and JSTARS. Currently, he serves as an Associate Editor for radar remote sensing of the IEEE TRANSACTIONS ON GEOSCIENCE AND REMOTE SENSING and the Editor-in-Chief of MDPI Sensors. He was rated as Most Cited Chinese Researchers by Elsevier.



Yuxin Gao received the master's degree in information and communication engineering from the School of Electronics and Information, Northwestern Polytechnical University, Xi'an, China.

Her research interests include interferometric synthetic aperture radar (SAR) and image processing, with application to remote sensing.



Rui Guo (Member, IEEE) received the B.S. and Ph.D. degrees in electronic engineering from Xidian University, Xi'an, China, in 2007 and 2012, respectively.

From 2012 to 2014, she was a full-time Postdoc Research Fellow with the Remote Sensing Technology Institute in German Aerospace Center (DLR), Cologne, Germany. She is currently an Associate Professor with the School of Automation, Northwestern Polytechnical University, Xi'an, China. Her research interests include polarimetric SAR, interferometric SAR, lidar, and application in remote sensing.